



# Kent Academic Repository

Smith, Michael D., Ramachandran, Babulakshmanan, Krishna, Krithi and Jyothy, S. N. (2025) *The effect of opening angle on shock patterns in supersonic jets*. *Monthly Notices of the Royal Astronomical Society*, 541 (4). pp. 3412-3426. ISSN 0035-8711.

## Downloaded from

<https://kar.kent.ac.uk/110910/> The University of Kent's Academic Repository KAR

## The version of record is available from

<https://doi.org/10.1093/mnras/staf1179>

## This document version

Publisher pdf

## DOI for this version

## Licence for this version

CC BY (Attribution)

## Additional information

## Versions of research works

### Versions of Record

If this version is the version of record, it is the same as the published version available on the publisher's web site. Cite as the published version.


### Author Accepted Manuscripts

If this document is identified as the Author Accepted Manuscript it is the version after peer review but before type setting, copy editing or publisher branding. Cite as Surname, Initial. (Year) 'Title of article'. To be published in **Title of Journal**, Volume and issue numbers [peer-reviewed accepted version]. Available at: DOI or URL (Accessed: date).

### Enquiries

If you have questions about this document contact [ResearchSupport@kent.ac.uk](mailto:ResearchSupport@kent.ac.uk). Please include the URL of the record in KAR. If you believe that your, or a third party's rights have been compromised through this document please see our [Take Down policy](https://www.kent.ac.uk/guides/kar-the-kent-academic-repository#policies) (available from <https://www.kent.ac.uk/guides/kar-the-kent-academic-repository#policies>).

# The effect of opening angle on shock patterns in supersonic jets

Michael D. Smith<sup>1,2</sup> ,<sup>1,2</sup> Babulakshmanan Ramachandran,<sup>2</sup> Krithi Krishna<sup>2</sup> and S. N. Jyothy<sup>2</sup>

<sup>1</sup>Centre for Astrophysics & Planetary Science, The University of Kent, Canterbury, Kent CT2 7NH, UK

<sup>2</sup>Department of Physics, Amrita School of Physical Sciences, Amrita Vishwa Vidyapeetham, Amritapuri Campus, Kollam, Kerala 690525, India

Accepted 2025 July 15. Received 2025 May 26; in original form 2024 December 21

## ABSTRACT

The initial opening angle of an astrophysical jet is a key indicator of the downstream shock configuration and kinetic efficiency. We analyse here the relationship for hydrodynamic jets of high pressure issuing from a circular nozzle. A jet can eventually settle down, after the initial penetration, into a divergent-convergent shape that forms one of two well-known shock patterns described as shock diamonds and Mach shock discs. The distance and shape of the standoff shock are investigated here through numerical simulations. As the opening angle increases, the standoff distance to the first shock generally occurs further from the nozzle, reaching a maximum, and then decreasing. A total of six distinct flow patterns are recognized. We establish semi-empirical formulae to link the physical parameters to the flow pattern. Large opening angles with Mach shock discs and subsequent plumes provide an interpretation for jet structures such as wide-angle FR I and stunted FR 0 radio galaxies. This can occur even when the jet is pressure matched to the ambient medium. In this case, a half-opening angle of  $16^\circ$  is found, beyond which at least the spine of the jet does not remain supersonic. Remarkably, this angle is a tight prediction, independent of Mach number. These results inform discussions of astrophysical jets as well as the release of gas in other contexts. It should be noted that we limit the study to non-relativistic hydrodynamics of adiabatic flow into a uniform medium. Relaxing these constraints requires extensive further studies.

**Key words:** hydrodynamics – shock waves – stars: jets – ISM: jets and outflows – galaxies: jets.

## 1 INTRODUCTION

The flow of gas exiting a circular nozzle at supersonic speeds has been the subject of many investigations covering diverse aspects (e.g. Adamson & Nicholls 1959; Tam 1995; Martí, Perucho & Gómez 2016). The pattern of shock waves is related to the overpressure and Mach number as well as other parameters (e.g. Franquet et al. 2015; Duronio, Villante & De Vita 2023; Smith & Richards 2023). With the high spatial resolution afforded by modern laboratory techniques and telescopes, it is of interest to deduce the jet parameters from an observed shock pattern. This can lead to enhanced interpretation and modelling in the astrophysical context.

A uniform parallel flow out of a circular nozzle into a vast gas reservoir provided the basis for our first computational study (Smith & Keogh 2022). We assumed an internal Mach number of 2 and various overpressures and densities. The jet drills through the environment leaving behind the exhaust, the field near the nozzle, which settled down to reach a final flow structure. The type of flow and shock pattern was then elucidated by also varying the Mach number up to Mach 8 (Duronio et al. 2023; Smith & Richards 2023).

However, it can be argued that these results are limited because observed astrophysical jets are invariably not parallel but possess significant opening angles. Therefore, our purpose here is to introduce a spraying jet, to determine how the spray alters the size and shape

of the flow pattern. In addition, nozzles with an adjustable opening angle are an integrable part of modern supersonic aircraft engines which enable optimum performance at different speeds and altitudes (Michel 2011).

Our main aim here is to elucidate how the opening angle alters the shock location and configuration. The interaction with the environment in terms of noise and mass advection is also of interest. To achieve this, we perform a range of simulations in which the jet is evolved for long times within a large reservoir. We then analyse the region close to the nozzle where we can confirm that the ambient pressure is maintained close to the original value but may contain natural disturbances, especially in terms of jet-induced noise and long-lived vortices. We also assume adiabatic inviscid flow which reduces the time and length-scales to those derived from the jet radius and ambient sound speed. The flow pattern and behaviour are then fixed by non-dimensional numbers, implying that the results are valid on any scale where the Navier–Stokes equations are appropriate.

Supersonic gas jets have properties that may help to identify them from a distance. In particular, if they are overpressured, they begin by diverging before converging to create a diamond shock pattern with intense hot spots along the axis. Such jets are termed equivalently overpressured and under-expanded.

If the jet pressure exceeds some critical value, a disc-shaped shock intercepts and reflects the converging shock, as illustrated in Fig. 1. This generates a reflected shock at a triple point (i.e. circle in axial symmetry) where the three shocks meet. The distance to the shock and the disc radius depend on the Mach number and overpressure

\* E-mail: [m.d.smith@kent.ac.uk](mailto:m.d.smith@kent.ac.uk) (MS); [ramachandranb@am.amrita.edu](mailto:ramachandranb@am.amrita.edu) (BR); [jyothysnair@am.amrita.edu](mailto:jyothysnair@am.amrita.edu) (SJ)

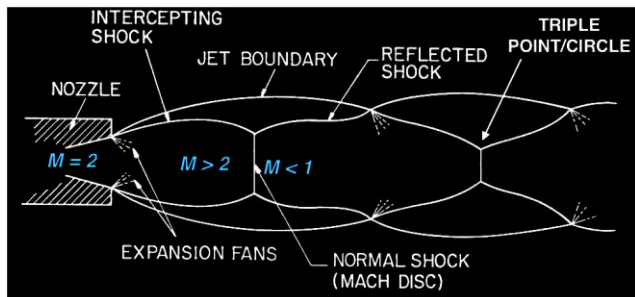


**Figure 1.** Some common terminology is used to describe the flow pattern when Mach discs are present. The Mach disc radius is often referred to as height, a left-over from planar analyses. Here, we are studying a cross-sectional profile, and the triple point is actually a circle (see Fig. 1). Note also that in planar flow, the term Mach stem is employed. In one dimension, the shock front is termed a Mach stem, and it connects to incoming and outgoing oblique shocks at a triple point. In two dimensions, we call it a Mach disc. However, it is generally slightly warped and not a flat disc. Taken and modified from Adamson & Nicholls (1959).

(Franquet et al. 2015; Smith & Richards 2023). In this respect, it was shown that the relative density mainly influences the frequency at which the oscillations in the pattern occur. Examples of these patterns are shown in Fig. 2.

Measured opening angles of astrophysical jets correspond to the visible jet, which depends on the radiation mechanism. The definition of jet width invariably relies on the chosen flux threshold unless there is a sharp boundary for which detected and physical edges correspond. Projection effects also have to be accounted for since the orientation to the line of sight is often unknown. We also would like to identify and measure the angle as close as possible to the base of the jet before it penetrates deeply into the surrounding medium. However, the location of the jet base and its interpretation as a nozzle may not always be appropriate.

What angles should we consider? The opening angles of jets from young stars are typically in the range  $\sim 5^\circ - 10^\circ$  on the micro-jet scale of  $\sim 0.01$  pc (Mundt & Fried 1983). On larger scales, the jets are wider but the opening angle decreases (Mundt, Ray & Raga 1991). More generally, protostars drive bipolar molecular outflows which widen as the protostar evolves, lying between  $\sim 10^\circ$  and  $70^\circ$  in some surveys (Hsieh, Lai & Belloche 2017) but not in others (Davis et al. 2009). Note that we will consider half-opening angles,  $\theta$ , up to  $36^\circ$  which covers both narrow and wide jets.

The sources of the other main class of jet are active galactic nuclei (AGNs). Radio VLBA data reveal the collimation zone in which a wide parabola transitions into an outer conical jet, as confirmed in the accumulated data presented by Kovalev et al. (2020). The full conical opening angles are mainly in the range  $\sim 2^\circ - 30^\circ$ . The data are consistent with the conical jet then entering a medium with a shallow pressure gradient and so becoming overpressured (Kovalev et al. 2020). A standing shock is then predicted as being possible just beyond the Bondi radius of the order of 100 parsecs. This is the scenario we envisage here except in an idealized form so that we can probe the problem systematically. Hence, we omit relativistic, magnetic, rotational, and pressure gradient contributions beyond the Bondi radius as a first stab at understanding the transition zone. This set up leads to stationary shocks (Levinson & Globus 2017) such as found in M87 (Hada et al. 2024). It should be noted that if the jet is in pressure equilibrium well within the Bondi radius, but then transits into an ambient medium with a shallow pressure gradient beyond this Bondi radius, it may well be underpressured as it overexpands in

the new surroundings. Standing shocks and jet disruption may then occur.

It should be noted that the observed jets associated with young stars and AGNs will usually involve additional physics, chemistry, and dynamics. Nevertheless, it remains vital to first understand the simplest scenario before simulating the more complex. We begin in Section 2 by presenting definitions, and outlining the simulations set up, including the implementation of the opening angle. The results for overpressured jets and for spraying pressure-matched jets are then provided in Section 3. An analysis is presented and implications are discussed in Section 4.

## 2 METHOD

### 2.1 Physical set-up

We wish to simulate an ideal gas that flows constantly at a supersonic speed out of a circular orifice in a wall. The ambient medium is initially uniform. The media are adiabatic and inviscid hydrodynamic fluids (without magnetic fields). These are generally well modelled by finite volume codes. A narrow boundary layer forms between the two fluid phases (jet and interface medium) across which there is high velocity shear and dissipation through numerical viscosity.

We present here exclusively 2D simulations. This is valid since our analysis is limited to the region near the nozzle. This should not be a limiting factor provided perturbations to the cylindrical symmetry do not grow in this region before being advected downstream. We have checked with several exploratory 3D runs of similar resolution and with small precession angles which indicate that 2D is sufficient to at least  $30R_{\text{jet}}$  (Smith et al., in preparation).

We scale the units of our simulation as follows.

- (i) The pressure and density units  $p_{\text{amb}}$  and  $\rho_{\text{amb}}$  together yield  $c_{\text{amb}}^2 = \gamma p_{\text{amb}} / \rho_{\text{amb}}$ .
- (ii) For the jet equivalents we use:  $p_{\text{jet}} = \kappa p_{\text{amb}}$  and  $\rho_{\text{jet}} = \eta \rho_{\text{amb}}$ , so that the jet sound speed is given by  $c_{\text{jet}}^2 = (\kappa/\eta)c_{\text{amb}}^2$ .
- (iii) Following the start of the simulation, we increase the jet velocity linearly with time to a final value of  $v_{\text{jet}}$  at time  $t = 10t_a$ . This yields a final Mach number of  $M = v_{\text{jet}}/c_{\text{jet}}$ .
- (iv) The code is set up by taking normalized units. The jet radius is set to  $R_{\text{jet}} = 1$ . By fixing the initial ambient sound speed also to one, the unit of time, given as the jet radius crossing time at the local speed of sound, is  $t_a = 1$ .
- (v) The initial ambient density is  $\rho_{\text{amb}} = 1$ , and ambient pressure is  $p_{\text{amb}} = 1/\gamma = 0.6$ , since we assume a monatomic gas.
- (vi) The velocity at the nozzle has two components since we assume here that there is no rotation. A conical expansion with half-opening angle  $\theta$  is assumed of the form

$$v_{\text{jet},z}(r) = v_{\text{jet}} \times \cos(\theta \ r/R_{\text{jet}}) \quad (1)$$

$$v_{\text{jet},r}(r) = v_{\text{jet}} \times \sin(\theta \ r/R_{\text{jet}}), \quad (2)$$

in cylindrical units. Note that the angle  $\theta$  is the spray angle from the circular nozzle and these relations are applied to transform into cylindrical coordinates.

(vii) To track the gas issuing from the jet nozzle, we implement a tracer field. The tracer takes a value of 1 for injected gas and zero for the original ambient material. It is then subsequently recorded as a mass-weighted tracer,  $\chi$ .

All the parameters including pressure and density could vary across the cross-section at the nozzle depending on the upstream conditions. For example, an expanding but concave hydrodynamic

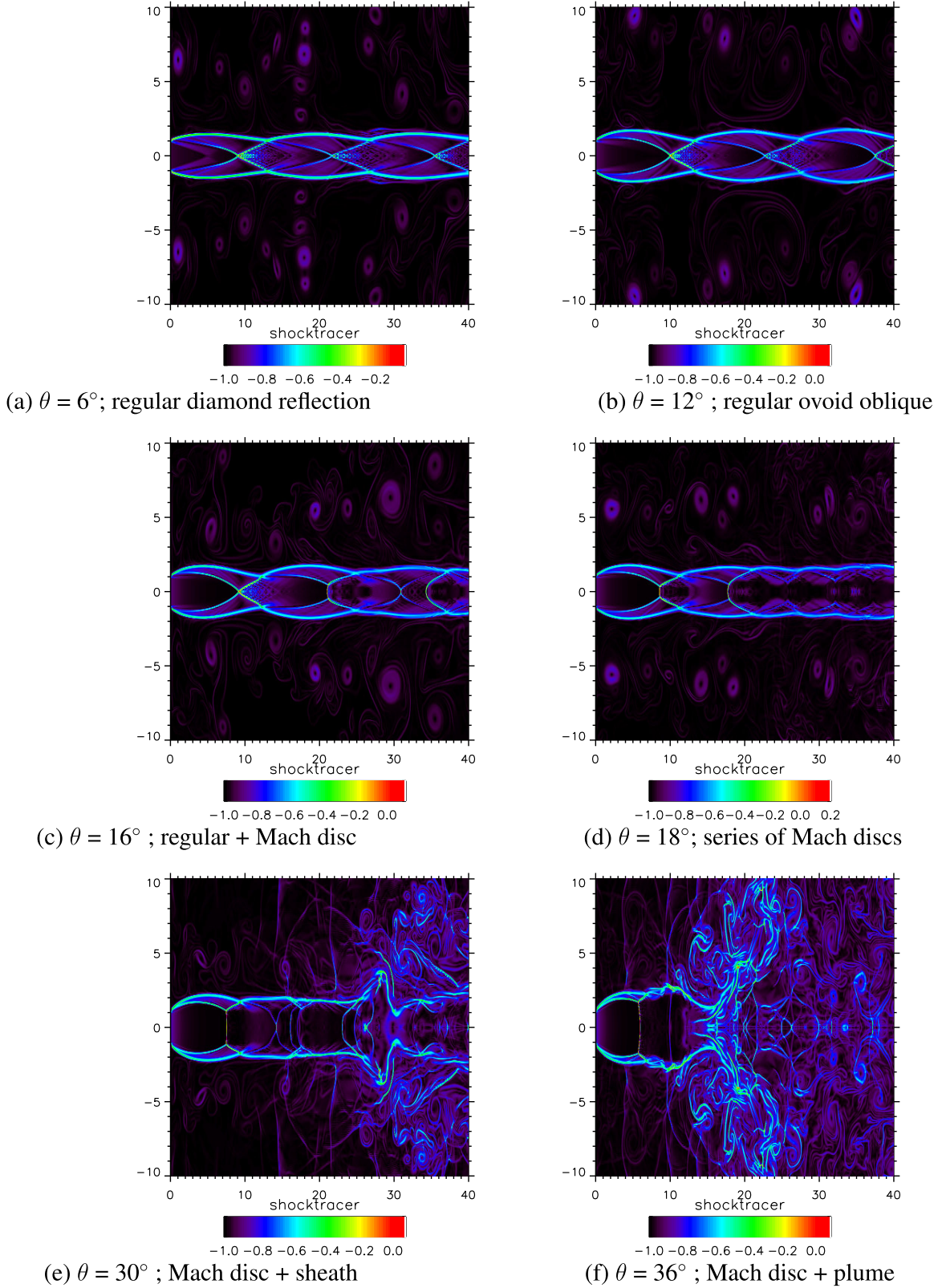


**Figure 2.** Dependence on opening angle. Six distinct flow patterns found in simulations in which only the half-opening angle is altered. Jets enter with a low overpressure of  $\kappa = 2$ , Mach number  $M_{\text{jet}} = v_{\text{jet}}/c_{\text{jet}} = 4$ , and relative density  $\eta = \rho_{\text{jet}}/\rho_{\text{amb}} = 0.5$ . Displayed are edge-on slices in which neighbouring zones of high relative pressure difference are combined with an interface recognition mechanism. This amplifies shock jumps and interfaces, to elucidate flow patterns. All panels are snapshots at time  $200 R_{\text{jet}}/c_{\text{amb}}$ . Note that, since we impose axial symmetry, these images are generated through reflection of the upper half of the slice to aid illustration.



jet would possess a lower pressure on the jet axis (Smith & Norman 1981). In addition, the radial velocity profile could be complex with shear and can be modelled by a Bernoulli constant across that values across the jet (Smith 1994). Hence, here we are assuming that the opening angle and overpressure are the determining factors.

## 2.2 Computational set-up

The astrophysics code *PLUTO*, incorporating Godunov-type shock-capturing schemes, was applied to the problem. It is freely distributed (Mignone et al. 2007).<sup>1</sup> Having experimented with solvers and resolutions in previous papers in this series, we chose between fast linear interpolation time-stepping Riemann solvers available in the *PLUTO* suite. We found that AUSM +, an advection upstream splitting method, to be preferred to the Harten, Lax, and Van Leer scheme detailed by Toro, Spruce & Speares (1994; denoted HLLC) since it proved to be more reliable close to the lip of the nozzle. The AUSM + Courant–Friedrichs–Lewy (CFL) recommended value of 0.4 was adopted.

We allow each simulation to evolve well beyond the time for the flow pattern to approach a quasi-steady state in the near field. However, a completely steady pattern is rarely achieved due to a combination of oscillations, surface waves, and turbulence. Hence, we quantify the parameters for the final pattern in terms of a mean value and oscillation amplitude.

The final pattern is found by allowing the jet to evolve into an atmosphere that is effectively an infinite reservoir. The transient waves are usually dispersed by  $100 t_a$  but we allow all runs to go to  $200 t_a$  and consider oscillations over the final  $10 t_a$  to estimate the unsteady nature of the final states. In addition, we produce space-time diagrams and movies to confirm the results.

Boundary conditions in the cylindrical coordinates  $(r, z)$  are as follows. Reflection at  $z = 0$  is imposed at the wall, outside of the hole from which the jet enters. Reflection is also required at  $r = 0$  on the  $Z$ -axis to ensure axial symmetry. At the outer edges, we take a free outflow condition. We have found that this is generally not adequate in the long term since the ambient pressure can build up uniformly to any level since there is no pressure gradient across a free outflow boundary. We have previously found this to occur at high Mach numbers and high overpressures if the reservoir is not adequately extended. Hence, we extend the surroundings to such a degree that the original far-field material is not overwhelmed.

The inner uniform cylindrical grid comprises 200 radially distributed zones and 800 axial zones. This converts into  $10 R_{\text{jet}}$  and  $40 R_{\text{jet}}$ , respectively. A much larger region in which the zones are stretched in a geometric series is added. This consists of 100 radially distributed zones and 200 axial zones. This converts into  $60 R_{\text{jet}}$  and  $140 R_{\text{jet}}$ , respectively. The ratios of the geometric series are 1.03656 radially and 1.018 1600 axially which yields zone sizes of  $0.05 R_{\text{jet}}$  up to the edge of the uniform region, which then stretches to  $1.814 R_{\text{jet}}$  and  $1.835 R_{\text{jet}}$  at the far outer radial and axial boundaries, respectively.

The outer gas reservoir is necessary to ensure that the jet has not entirely altered the atmosphere. This is evident in Fig. 3, which displays the inner uniform region on the left and the entire simulated region on the right. It is clear that the region with uniform resolution has been fully disturbed, while the reservoir is still close to its pristine condition even after  $200 t_a$ . In this example with a low opening angle, we show the density and the jet tracer.

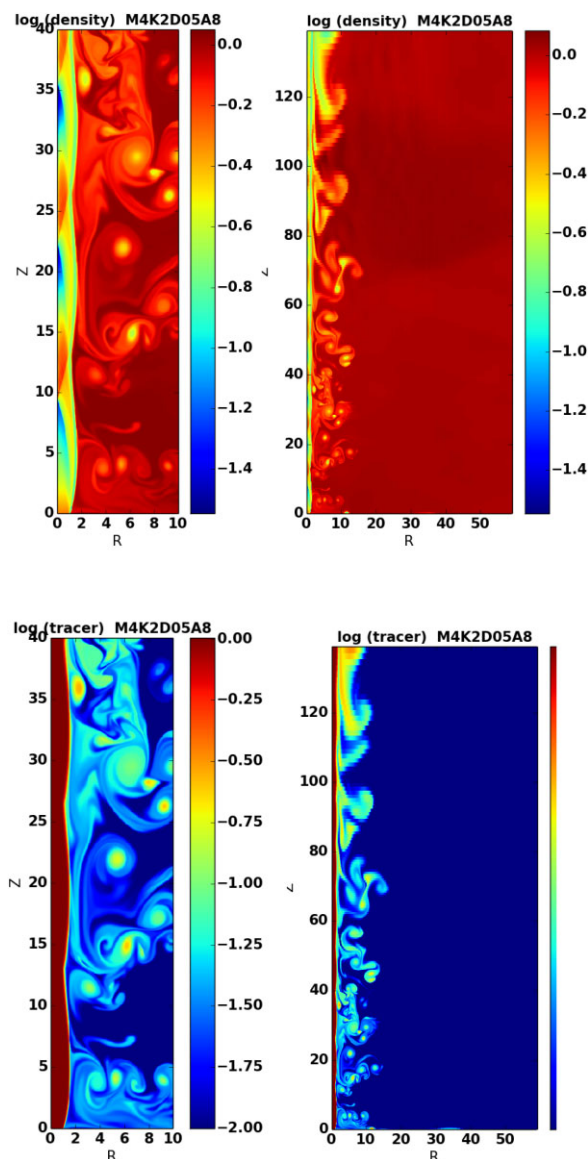


**Figure 3.** For a half opening angle  $\theta = 8^\circ$ , the distributions of density (upper) and jet tracer (lower panels) across the uniform grid section (left) and the entire simulated domain (right panels). This is for a Mach 4,  $\kappa = 2$  and  $\eta = 0.5$  at time  $200 t_a$ .

We need to ensure that the reservoir can cope with quite high opening angles and jet pressures. We display the pressure (upper panels) and tracer (lower panels) distributions for a jet with a wide opening angle in Fig. 4. This demonstrates a well-developed downstream turbulent plume. Although pressure fluctuations continue in the uniform-zoned region, large systematic variations are transmitted into the extensive reservoir which continue to be smoothed out even after  $200 t_a$ .

A number of movies have been archived in a *Zenodo* repository at <https://zenodo.org/records/14174127> i.e. with DOI 10.5281/zenodo.14174127. A summary of the simulations and the archived movies is provided in Table 1. These movies of the pressure distribution show not only the general steadiness of the stand-off shock but also elucidate the variability downstream as surface instabilities take over. This results in disturbances in the ambient medium, which then feed back pressure waves upstream, towards

<sup>1</sup><http://plutocode.ph.unito.it/>

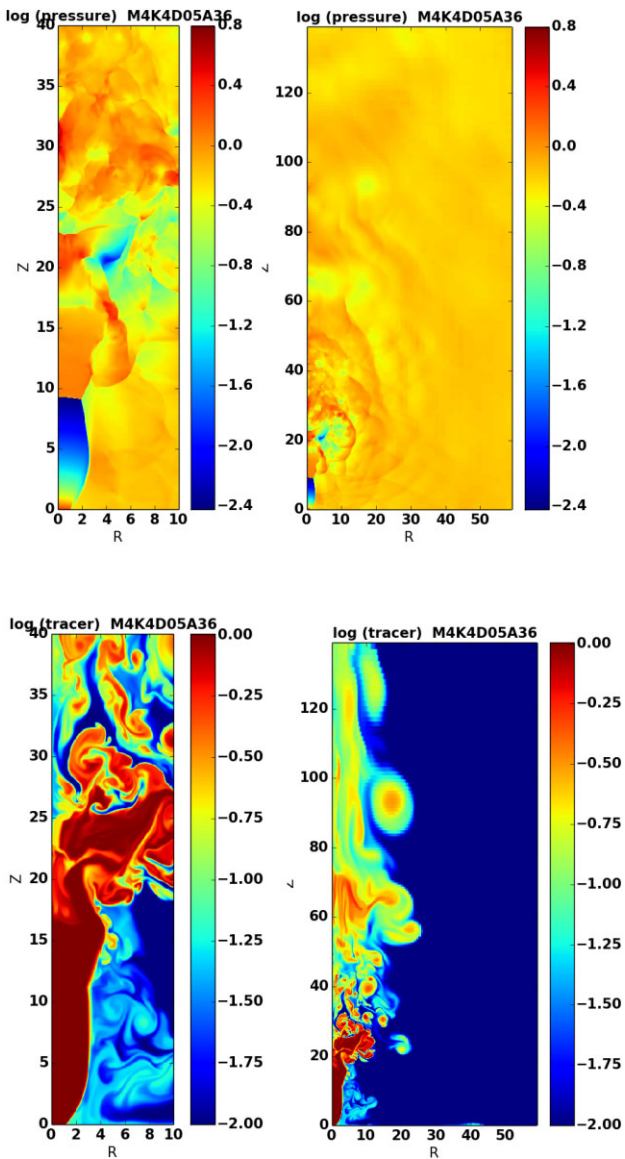


**Figure 4.** For a half opening angle  $\theta = 36^\circ$ , the distributions of pressure (upper) and jet tracer (lower panels) across the uniform grid section (left) and the entire simulated domain (right panels). This is for a Mach 4,  $\kappa = 4$  and  $\eta = 0.5$  at time 200 units.

the nozzle. The stand-off shock then accordingly adjusts, often in the form of irregular oscillations.

### 3 RESULTS

#### 3.1 Example flow patterns: Mach 4, $\kappa$ 2, $\eta$ 0.5 jet

The first aim is to distinguish opening angles that generate diamond shock patterns from Mach shock discs. To begin, we executed 19 runs with Mach number  $M = 4$  and pressure ratio  $\kappa = 2$ , in which we increased the angle  $\theta$  from zero to  $36^\circ$  in increments of  $2^\circ$ . Six shock configurations are identified from these runs, as illustrated in Fig. 2.

Crucial flow features are as follows:

(i) Regular reflection: a flow that contains only oblique shocks (panels (a) and (b) of Fig. 2).

**Table 1.** Summary of simulations presented in this paper and the specific half-opening angles for which movies are archived at DOI 10.5281/zenodo.14174127.

Figure number	Mach number	Pressure ratio $\kappa$	Density ratio $\eta$	Half-opening angle $\theta$
10, 11(upper)	2	1	0.5	$16^\circ$
14	2	6	0.5	$8^\circ$
12, 13(upper)	3	4	0.5	$12^\circ$
10, 11(middle)	4	1	0.5	$16^\circ$
10, 11(middle)	4	1	0.5	$24^\circ$
2(a)	4	2	0.5	$6^\circ$
2(b), 6(upper)	4	2	0.5	$12^\circ$
2(c)	4	2	0.5	$16^\circ$
2(d)	4	2	0.5	$18^\circ$
2(e)	4	2	0.5	$30^\circ$
2(f)	4	2	0.5	$36^\circ$
6(lower)	4	2	0.5	$20^\circ$
12, 13(middle)	4	4	0.5	$12^\circ$
15	4	6	0.5	$8^\circ$
15	4	10	0.5	$8^\circ$
12, 13(lower)	5	4	0.5	$12^\circ$
10, 11(lower)	6	1	0.5	$16^\circ$
15	6	6	0.5	$8^\circ$

(ii) Shock diamonds: conical shocks that reflect off the jet axis to appear as a diamond pattern in projection (panel (a) of Fig. 2). A series of several diamonds can occur in the near-field, also commonly termed Mach diamonds or thrust diamonds (panel (a)).

(iii) Ovoid reflection: identified here with curved oblique shock surfaces which as repeated ovals downstream (panels (b) and (c)).

(iv) Mach shock cisc: a disc-shaped shock with the shock surface normal to the flow on the axis (panels (d)–(f)).

(v) Repeated mach discs: small discs appearing close to jet spine (panel (d)).

(vi) Mach disc with sheath: large disc with fast jet sheath, becoming turbulent downstream (panel (e)).

(vii) Full mach disc: normal shock crosses flow followed by a turbulent plume (panel (f)).

In addition, we find here that there is a critical opening angle in which the stand-off shock is in transition from regular to Mach reflection (panel (c)). Hybrid fluctuating flow patterns exist close to this angle. An example of the physical state on the uniform grid at the end of the run is shown in Fig. 5 for  $\theta = 16^\circ$ . Note that the ambient pressure (lower-right panel) is smooth although the density (upper left panel) contains numerous knots (thin vortex rings) of entrained hot, low density jet gas. The jet itself possessed a slightly extended diamond shock while the downstream shocks are small Mach discs. Note that despite the axial discs, a high-speed jet is maintained, as shown in the upper-right panel of Fig. 5.

To determine the angle at which the flow transits from regular to Mach disc from the simulations, we model the zones where the oblique incident shock switches to the reflected shock either on the axis or via a triple point. To more accurately determine the location where the incident and reflected shocks meet, we apply a second-order fit to the zonal values. Typical analysed shock structures for these two distinct configurations are illustrated in Fig. 6 for regular reflection (upper panel) and Mach reflection (lower panel).

Measurement of the Mach disc radius is achieved as follows. We determine the radial distance of the incident and reflected shocks as a function of the axial distance. The approximate zone location where they intercept is then determined. We then fit a parabola near

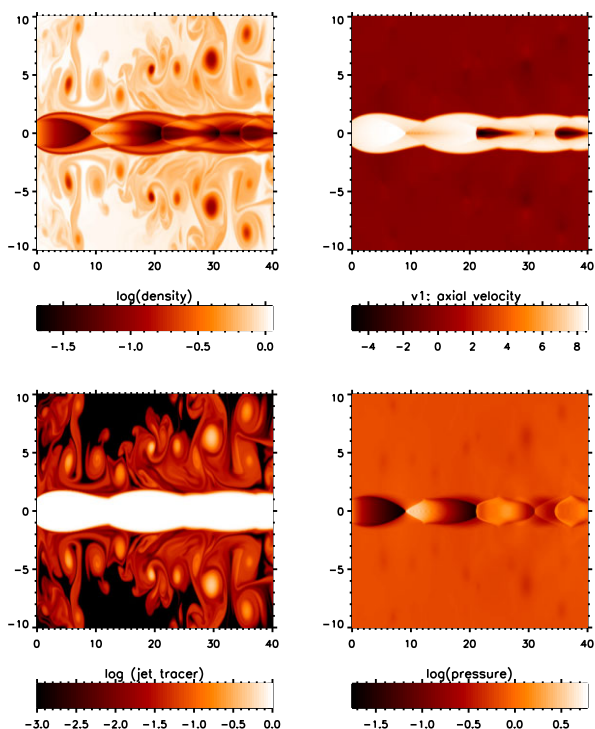


**Figure 5.** The distributions of physical parameters for a Mach 4 jet with half-opening  $\theta = 16^\circ$ , overpressure  $\kappa = 2$ , and density ratio  $\eta = 0.5$ . The time corresponds to the end of the run at  $t = 200t_a$  where  $t_a = R_{jet}/c_{amb}$ . The length-scale is in units of the jet radius with the  $x$ -axis units contracted so that the flow fits into a square panel. Upper-left panel: density, upper-right panel: axial velocity component, lower-left: tracer for jet gas, lower-right: pressure.

this location to obtain the triple point coordinates. The location is then confirmed by inspection of Fig. 6 and checked by comparison to Fig. 2.

The shock radius as a function of the half-opening angle is displayed in Fig. 7 for the standard case. A clear division is found with regular reflection occurring for  $0^\circ \leq \theta < 16^\circ$ . The case with  $\theta = 0^\circ$  (no opening angle) was covered by Smith & Richards (2023) where for a parallel flow, it was established that regular reflection occurs for  $\kappa < 7.8$ . This behaviour is interpreted here and further detailed in Section 4. As the opening angle is increased from a small angle, the initial jet expansion is enhanced by the extra spraying. The inner jet cavity is relatively bloated. The diverging jet thus overexpands and the ensuing convergence is enhanced. Hence, the incident converging shock approached the axis at a steeper angle for higher initial opening angles.

However, a further increase in the nozzle opening angle has a large effect on the ram pressure. The jet momentum flux decreases rapidly with distance, and a strong perpendicular shock is required to raise it to the level of the ambient pressure. Hence, a jet with a sufficiently large opening angle will generate a Mach shock disc. Therefore, if regular reflection occurs at low opening angles, a critical shock angle should exist for which regular reflection is possible. The result is that Mach shock discs appear even at quite low  $\kappa$  for high opening angles.

The distance of the stand-off shock from the nozzle is measured along the jet axis by searching for the first significant increase in pressure. The pressure jumps can be visualized with a space-time diagram that displays the pressure along the jet axis for all data dumps. An example for the Mach 4 jet with  $\theta = 16^\circ$  is displayed

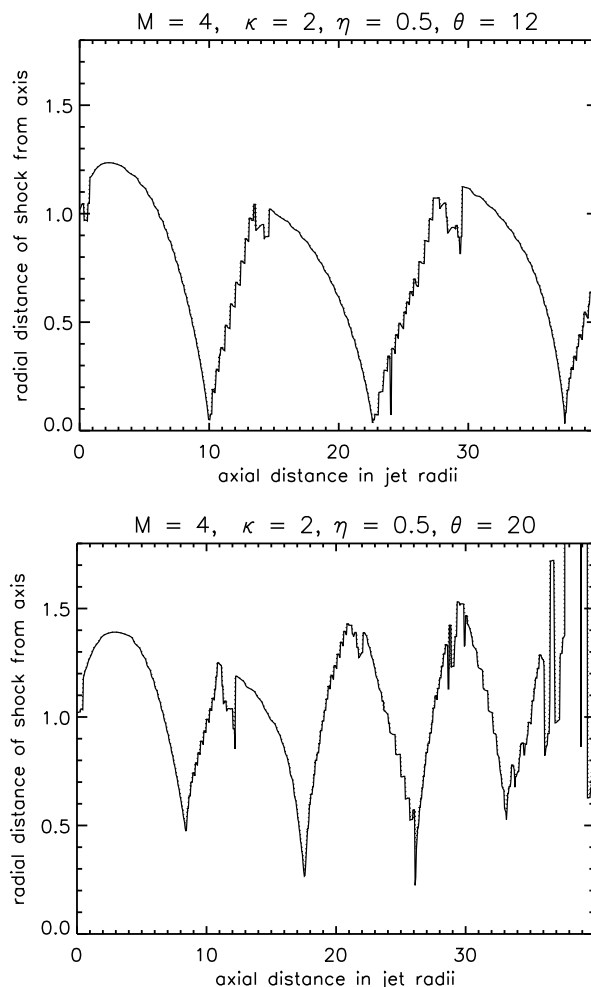


**Figure 6.** The radial distance of the oblique shock as a function of the axis coordinate for  $\theta = 12^\circ$  (upper panel demonstrating regular reflection) and  $\theta = 20^\circ$  (lower panel, where the oblique shocks do not extend down to the axis). Units are in jet radii. This is for Mach 4, density ratio  $\eta = 0.5$ .

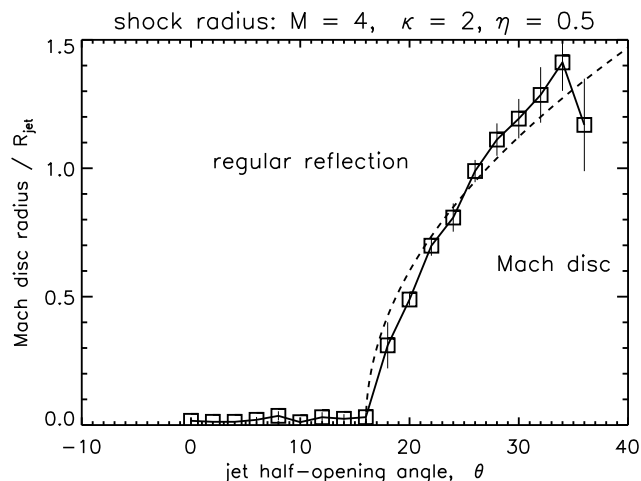


**Figure 7.** The radius of the Mach shock disc as a function of the half-opening angle,  $\theta$ , for an overpressure  $\kappa = 2$  for a jet with Mach number of 4 and density  $\eta = 0.5$ , as measured after 200 time units. The error bars correspond to the root-mean-square spread over the final 20 time units. The dashed line is the proposed fit from equation (5).



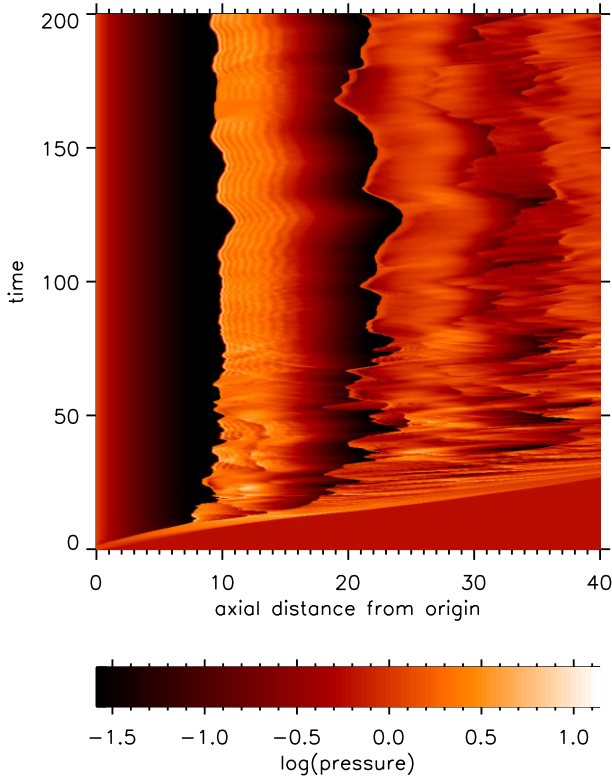


**Figure 8.** Space–time diagram for Mach 4 jets with  $\kappa = 2$ ,  $\theta = 16^\circ$  and initial density ratio  $\eta = 0.5$ . The distribution of the pressure along the jet axis ( $x$ -axis) is shown as function of the time ( $y$ -axis). Length-scale is in units of the jet radius.

in Fig. 8. This diagram illustrates that a quasi-steady flow pattern is achieved well before the end of the simulation. However, irregular oscillations occur in the locations where the shocks intercept the axis. The time-scale for the variations, of order 20 time units, is consistent with the surface waves propagating at the Kelvin–Helmholtz speed. This is the relevant speed at which the jet channel can alter shape. Taking into account the momentum flow rate across the interface, we employ the estimate

$$V_{\text{KH}} = v_{\text{jet}} \frac{\sqrt{\eta}}{1 + \sqrt{\eta}} \quad (3)$$

(Smith & Keogh 2022). In terms of the jet Mach number this becomes

$$V_{\text{KH}} = M_{\text{jet}} \frac{\sqrt{\kappa}}{1 + \sqrt{\eta}} c_{\text{amb}}. \quad (4)$$

The stand-off distance,  $D$  is plotted against the half-opening angle,  $\theta$ , in Fig. 9 for the parameters  $M = 4$ ,  $\kappa = 2$ , and  $\eta = 0.5$ . The oscillations have been used to calculate an error bar by finding the mean and root mean square of this distance over a time period appropriate for the oscillations as determined from space–time diagrams. We present root mean square variations by sampling over the final 20 time units.

Fig. 9 shows that, from the narrow  $y$ -axis range, the location of the stand-off shock only varies moderately as the opening angle increases. The distance  $D$  has a non-monotonic behaviour. There is a moderate increase of  $D$  with  $\theta$  at low  $\theta$  up to  $\theta \sim 12^\circ$ . In contrast, there is a linear decrease of  $D$  with  $\theta$  at higher  $\theta$ . The approximate linear fits will be detailed in Section 3.2.

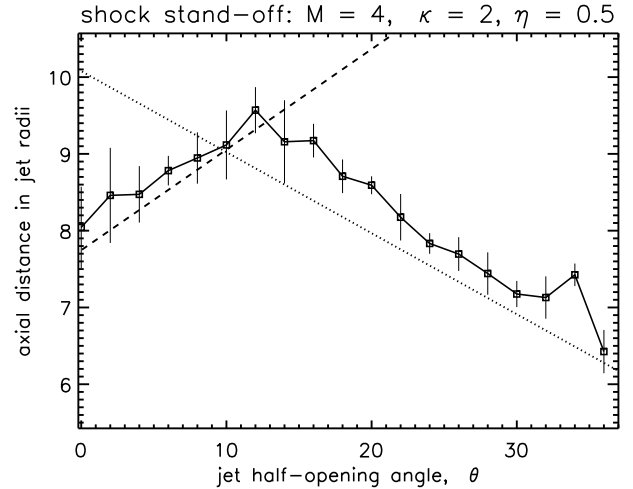


**Figure 9.** The distance,  $D$ , of the first shock along the jet axis as a function of  $\theta$ , in units of the jet radius. This is for Mach 4, density ratio  $\eta = 0.5$ . The error bars were determined from a root-mean-square fit covering the final 20 time units in order to account for oscillations.

It was noted above that the transition from regular reflection to Mach shock disc occurs at  $\theta \sim 16^\circ$ . This corresponds approximately to where the stand-off distance starts to decrease. This suggests that a large opening angle dilutes the ram pressure, causing the Mach disc to occur closer to the nozzle while a small opening angle has relatively little influence on the jet area before the stand-off shock is reached.

The transition occurs over  $\theta$  values in which dual solutions may be permitted analytically: both regular reflection and Mach shock discs are valid solutions. This result was found from theoretical modelling, where a uniform ambient pressure is assumed and no sound waves feedback on the jet (e.g. Courant & Friedrichs 1948). However, in practice, feedback from the ambient medium causes oscillations in the channel shape, as best seen in the associated movies which show that the flow pattern can fluctuate.

We find that the height of the Mach disc,  $H_{\text{MD}}$ , can be approximately represented by the formula

$$H_{\text{MD}} = 0.3 \times (\theta - 16)^\circ = 2.27 \times (\theta_{\text{rad}} - 0.279)^{1/2} \quad (5)$$

for a Mach number of 4, for  $\theta > 16^\circ$  in degrees and  $\theta_{\text{rad}} > 0.279$  in radians. This is shown as the overlaid dashed line in Fig. 7. With  $\kappa$  fixed at 2, we thus expect the height to be zero for small  $\theta$ , as shown in the figure. However, even with this low  $\kappa$ , the shock pattern transforms to a Mach disc configuration for  $\kappa$  exceeding  $\sim 16^\circ$ .

We are employing the simulations to develop insight into the relationship between the flow structure and the physical parameters. It should be noted that we are developing a semi-empirical formalism to quantify these non-linear hydrodynamic flows for the first time. Even the well-known relationships for stand-off distances and disc height remain largely empirical (see the review of Franquet et al. 2015). We thus begin with this fundamental case first to gain insight before going deeper.

### 3.2 The expanding pressure-matched jet

Jets with low values of overpressure are described as slender. This facilitates an understanding of the shock patterns. In particular, a jet which is close to being pressure-matched with  $\kappa \sim 1$  is an interesting case with the spreading jet providing the pressure imbalance beyond



the nozzle. A scenario like this in which a jet has propagated through an inner core within which the pressure falls with distance from the source is of interest. Specifically, the pressure gradient is assumed to be quite shallow so that the expanding jet has remained pressure matched. As this expanding jet gas exits the nozzle at supersonic speeds, it will at first become underpressured or overexpanded.

In our set-up, the gas exits the core, to meet the ambient medium in which there is no pressure gradient. This will be a good approximation provided the ambient pressure fall-off takes place on larger scales than that of the stand-off distance. This scenario was first advanced by Smith (1982) for wide-angle radio galaxies on the kiloparsec scale. It has recently been suggested in the context of relativistic jets on smaller scales (Kovalev et al. 2020).

Previously, the stand-off distance for parallel flows was quantified (Smith & Keogh 2022). In the case of zero opening angle, the distance of the stand-off shock scales in proportion to the Mach number for both regular reflection and Mach shock discs, as confirmed for the present set-up by Smith & Richards (2023). For any given Mach number, Mach shock discs occur at sufficiently high overpressures. At intermediate  $\kappa$ , however, neither flow pattern is accurate with the stand-off distance generally at some intermediate distance. Here, we determine if this holds for non-zero opening angles.

For the shock diamonds at low overpressures, simulations and analysis are consistent. For  $\theta = 0^\circ$ , the stand-off shock distance is approximately proportional to both the Mach number and overpressure in the regular reflection regime:

$$D_1(\theta = 0) = \sqrt{(M_{\text{jet}}^2 - 1)\kappa^\beta} R_{\text{jet}}. \quad (6)$$

where  $\beta \sim 1$ . All results presented here for  $\theta = 0^\circ$  follow this result.

We extend this result to small non-zero  $\theta$  which correspond to regular reflection. On inspection of the simulations with low  $\kappa$ , as shown in Fig. 10, a linear dependence on the opening angle is appropriate. We thus obtain the empirical formula

$$D_1(\theta) = D_1(\theta = 0) \times (1 + 0.5\theta(M_{\text{jet}}^2 - 1)^{1/2}/\kappa), \quad (7)$$

where angles are in radians. This is superimposed on all the stand-off figures here via the thick dashed lines.

At large angles, the trend reverses. The Mach disc intercepts the jet axis closer to the nozzle for wider initial openings. Analytical fits are less accurate but still provide some insight. Whereas the flow pattern of regular reflection is dependent on the means by which rarefaction waves propagate across the jet, the Mach shock disc depends on the ram pressure. For large opening angles, the momentum is spread and the ram pressure or thrust falls faster. Hence, the stand-off is positioned closer to the nozzle.

For a parallel jet at high overpressures, Smith & Keogh (2022) recovered the established Mach disc distance formula:

$$D_2(\theta = 0) = 1.38\gamma^{1/2}\kappa^{1/2}M_{\text{jet}}R_{\text{jet}}, \quad (8)$$

where  $\gamma$  is the specific heat ratio. This was successfully tested to determine if it applies to the higher Mach number range more relevant to astrophysical applications (Smith & Richards 2023). For those parallel flows, this formula was an excellent fit for Mach 2 jets. For high Mach numbers, there was some deviation with  $D_2$  about a factor of  $\sim 1.25$  larger (Smith & Richards 2023).

Searching for a similar formula, we insert a multiplicative factor:

$$D_2(\theta) = D_2(\theta = 0) \times (1 - 0.6\theta). \quad (9)$$

This relation is shown as dotted lines in the stand-off figures. We conclude that a good fit to the stand-off distance occurs for low  $\kappa$  values as displayed in Fig. 9 and the middle panel of Fig. 10.

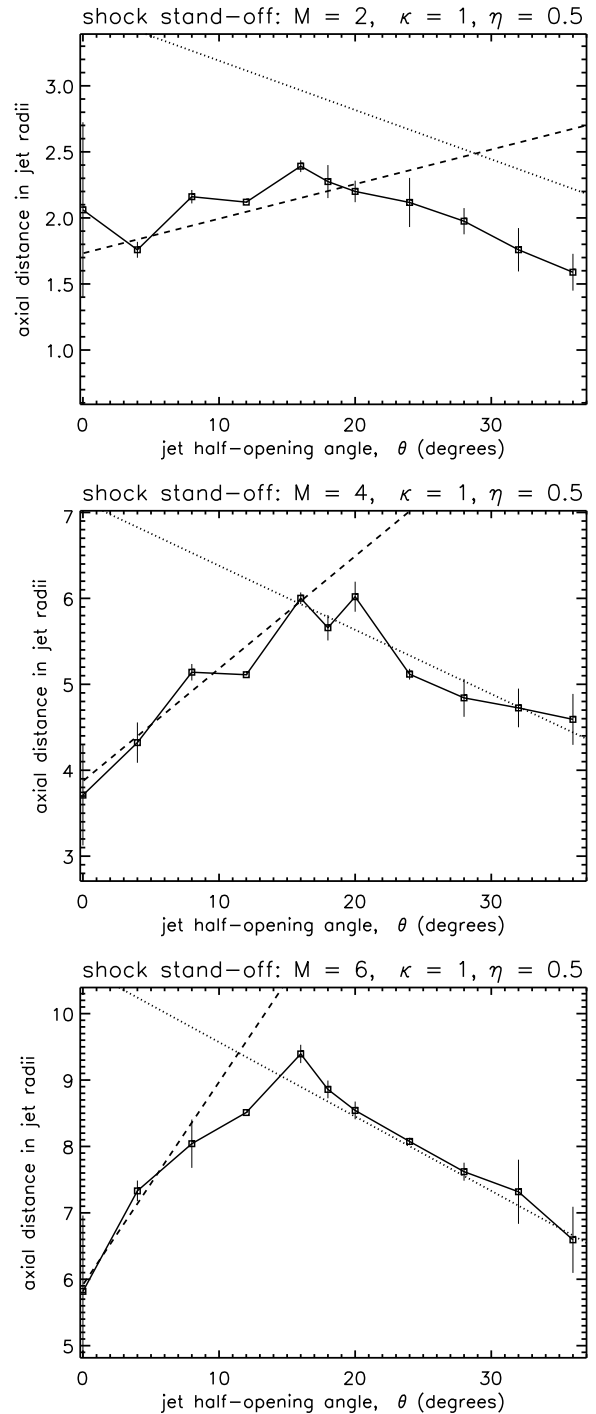


**Figure 10.** The stand-off distance for opening pressure-matched jets. The distance of the first shock along the jet axis as a function of  $\theta$ , in units of the jet radius. This is for Mach 2, Mach 4, and Mach 6,  $\kappa = 1$  and density ratio  $\eta = 0.5$ . The analytical power laws superimposed are those from equation (7; dashed line) and equation (9; dotted line). The error bars were determined from a root-mean-square fit covering the final 20 time units in order to account for oscillations.

The radii of the Mach disc for the  $\kappa = 1$  simulations are shown in Fig. 11. It is seen that the transition is sharp at  $\theta \sim 16^\circ$  for the higher Mach number jets. However, for the low Mach number case the transition is gradual with discs not extending across the entire jet until the largest of opening angles.

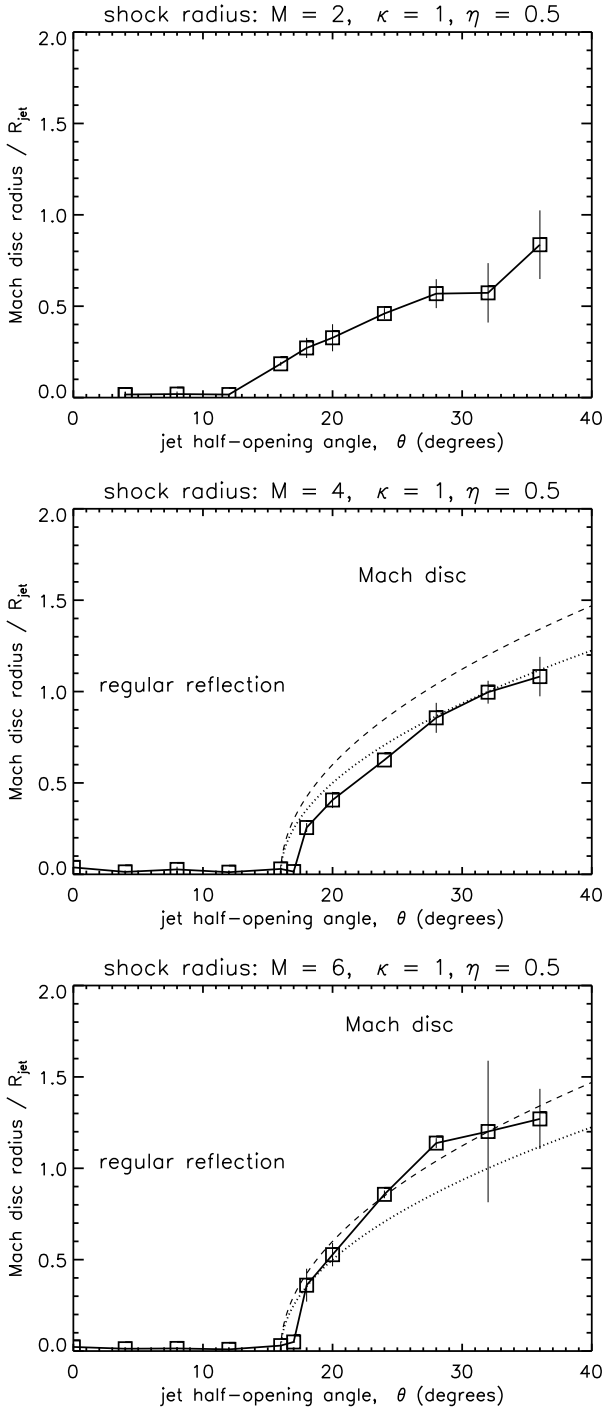


**Figure 11.** The radius of the Mach shock disc as a function of the half-opening angle,  $\theta$ , for an overpressure  $\kappa = 1$  for a jet with Mach numbers of 4 and 6, density  $\eta = 0.5$ , as measured after 200 time units. The error bars correspond to the root-mean-square spread over the final 20 time units. The dashed line is the proposed fit from equation (5).

The Mach 4 result in the middle panel of Fig. 11 follows the analytical fit

$$H_{\text{MD}} = 0.25 \times (\theta - 16)^{1/2}, \quad (10)$$

as shown by the dotted line. On the other hand, the Mach 6 case closely corresponds to the dashed line as given by equation (5) above.

In summary, the dominant flow pattern changes from regular to Mach reflection at  $\sim 16^\circ$ . This is also the angle corresponding to the knee in the stand-off distance as shown in Figs 10 and 11.

### 3.3 Higher overpressures

The stand-off dependence on opening angle for high overpressures is displayed in Fig. 12. Three Mach numbers are chosen with  $\kappa$  fixed at 4. Note that the figures are scaled so that for each Mach number the variation in stand-off distance is small in comparison to the distance from the nozzle.

In the regular reflection regime, there is no clear dependence on the opening angle for the Mach 4 and Mach 5 cases. The error bars that represent the time variability are as large as the changes due to the opening angle. The Mach 3 runs generate steadier flow patterns as seen in the available M3K4D05A12 movie in the [Zenodo repository](#) which shows a hybrid flow pattern.

The flow pattern switches to Mach disc at higher opening angles. The stand-off distance falls gradually with increasing angle and it is only at the largest opening angles that the distance of the Mach disc falls towards the analytical formula of equation (7) as given by the dotted lines in Fig. 12. This is essentially due to the variable behaviour at the transition between regular and Mach reflection at high Mach numbers as discussed by Smith & Richards (2023).

The equivalent distributions for the disc radius are plotted in Fig. 13. For Mach 3, regular reflection occurs only at low opening angles while for higher Mach numbers regular reflection is present up to  $\theta \sim 14^\circ$ . The previous formula, equation (5), provides a guide for comparison.

While these results indicate some trends with opening angle, the relationship with Mach number and overpressure needs clarification.

### 3.4 Mach number and overpressure

We study the flow pattern dependence on Mach number by fixing the opening angle and overpressure. For a parallel flow ( $\theta = 0^\circ$ ) and very low overpressures ( $\kappa \sim 1$ ), sound waves emanating into the jet from the lip of the nozzle make the angle  $\tan^{-1}(1/\sqrt{M_{\text{jet}}^2 - 1})$ . This leads to regular reflection with the sound waves crossing the axis at a stand-off distance of  $D = \sqrt{M_{\text{jet}}^2 - 1}$ . Thus the stand-off distance increases with the Mach number as the flow becomes more streamlined.

Smith & Keogh (2022) and Smith & Richards (2023) showed through simulations that this can be extended to higher overpressures with an approximately linear dependence on  $\kappa$ :  $D \sim \kappa \sqrt{M_{\text{jet}}^2 - 1}$ . This holds below an overpressure of

$$\kappa_{\text{tran}} \sim \kappa_M = 0.44(M_{\text{jet}}^2 + \frac{2}{\gamma - 1}), \quad (11)$$

as shown by Smith & Richards (2023).

On the other hand, at low Mach numbers and high overpressures, a Mach disc intervenes. The stand-off distance with  $\theta = 0^\circ$  is then given by equation (8) as confirmed by Smith & Richards (2023). An angular dependence has been added here as expressed by equation (9).

Now setting  $\theta = 8^\circ$ , the top panel of Fig. 14 shows that this still holds for low Mach numbers where the dotted line is the adopted analytical formula equation (9).

The lower panel of Fig. 14 reveals the flow pattern with regular reflection at high Mach numbers. There is an extended range of Mach numbers for which the pattern varies between this and the Mach

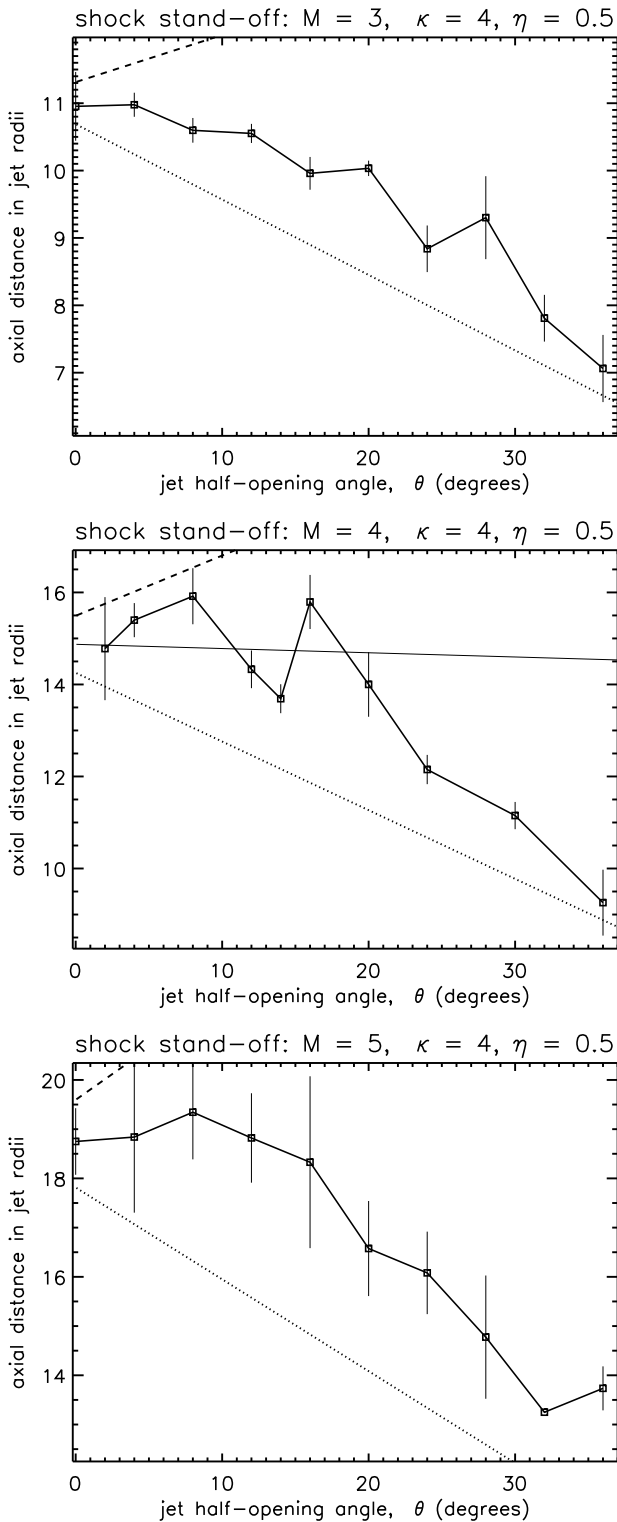


**Figure 12.** The distance of the first shock along the jet axis as a function of  $\theta$  for a fixed overpressure  $\kappa = 4$  and density ratio  $\eta = 0.5$ . Simulations were analysed for the three indicated Mach numbers. Units are expressed in jet radii. The error bars were determined from a root-mean-square fit covering the final 4 time units in order to account for oscillations. The analytical dotted line corresponds to the Mach disc relation, equation (9).

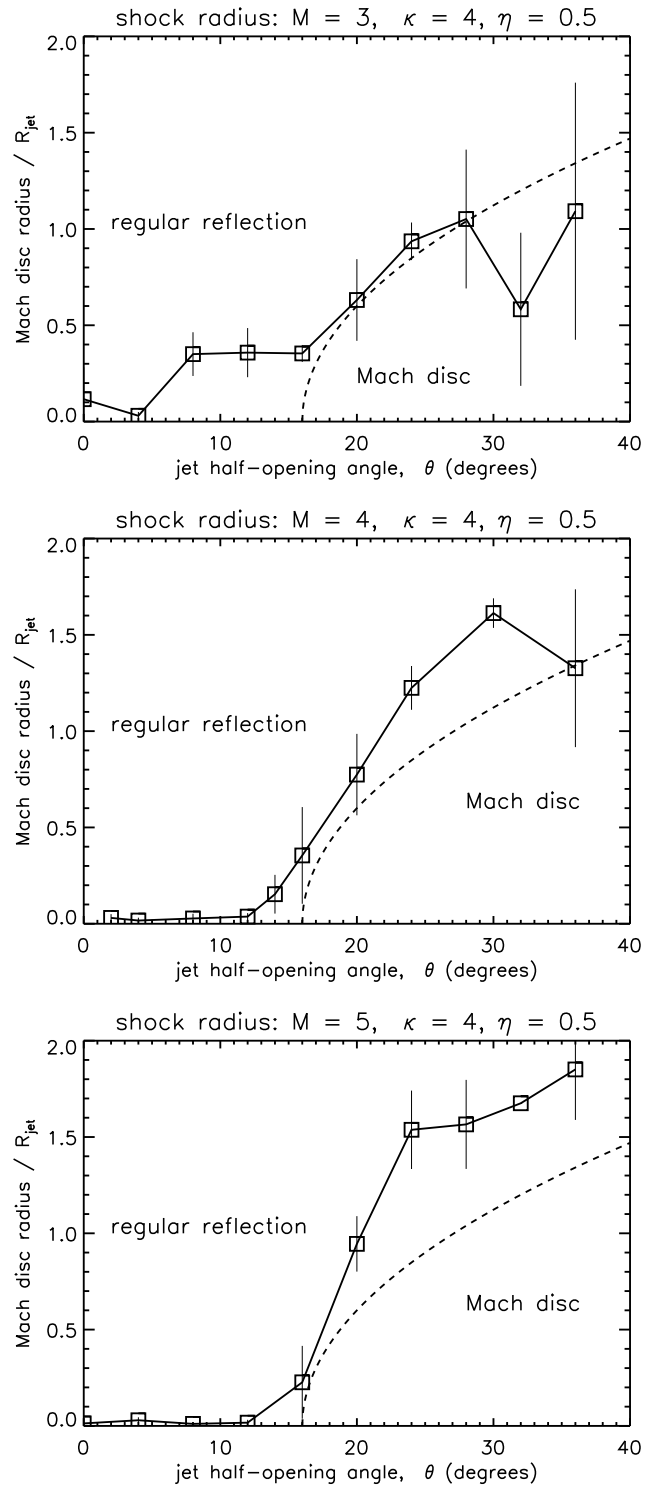


**Figure 13.** The radius of the Mach shock disc as a function of the half-opening angle,  $\theta$ , for an overpressure  $\kappa = 4$  for a jet with Mach numbers of 3 (upper), 4 (middle), and 5 (lower panel), and density  $\eta = 0.5$ , as measured after 200 time units. The error bars correspond to the root-mean-square spread over the final 20 time units. The dashed line is the proposed fit from equation (5).

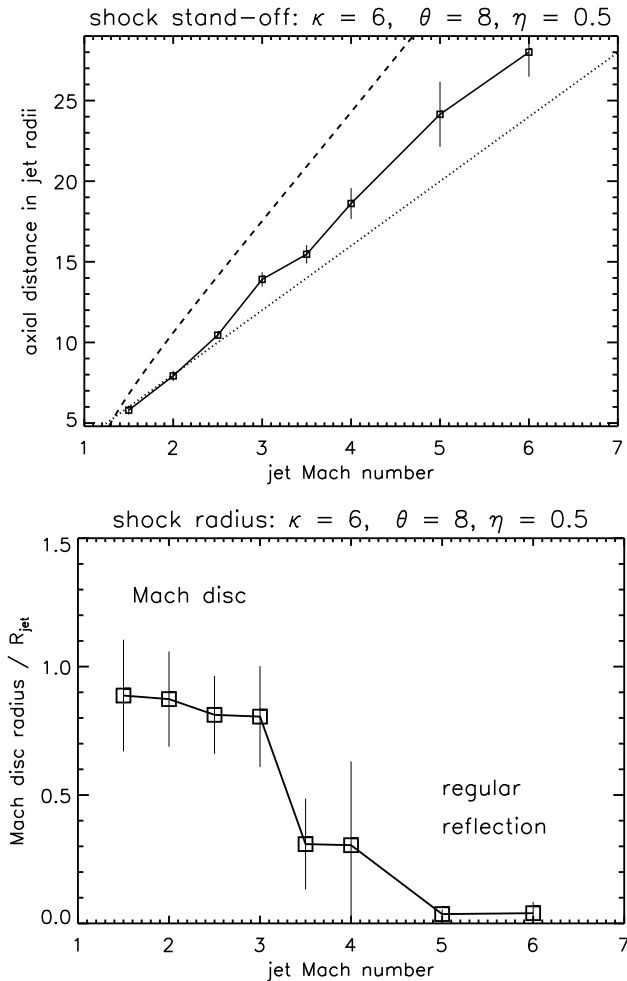


**Figure 14.** Dependence on Mach number. The distance of the first shock along the jet axis (upper) and Mach disc radius (lower panel) as a function of Mach number for half-opening  $\theta = 8^\circ$  in units of the jet radius with a jet density ratio  $\eta = 0.5$ . The error bars were determined from a root-mean-square fit covering the final 20 time units in order to account for oscillations. The stand-off distance relations for regular reflections, equation (7); dashed line) and Mach shock discs equation (9; dotted line) are superimposed.

disc configuration. The dashed line corresponding to equation (7) for regular reflection does not follow the data here. This is consistent with the high Mach number and overpressure results of Section 3.3.

The type of flow is revealed in Fig. 14, which shows the switch from Mach shock discs to regular reflection between  $M \sim 3$  and 5. This extended transition region is where the flow pattern is seen to oscillate, as indicated by the large error bars. Holding both the opening angle and Mach number constant, we ran a set of simulations in which the overpressure was adjusted. The stand-off distance for a Mach 4 jet is shown in the top panel of Fig. 15. The corresponding flow pattern is revealed through the Mach disc radius displayed in the lower panel.

At low overpressures, the stand-off distance now follows the relations as stated above (dashed line). However, for high overpressures, the flow structure appears quite turbulent as apparent from the error bars. This is clear in the lower panel of Fig. 15 for the Mach disc radius, which shows that the flow pattern varies between regular and Mach reflection at the high overpressures.

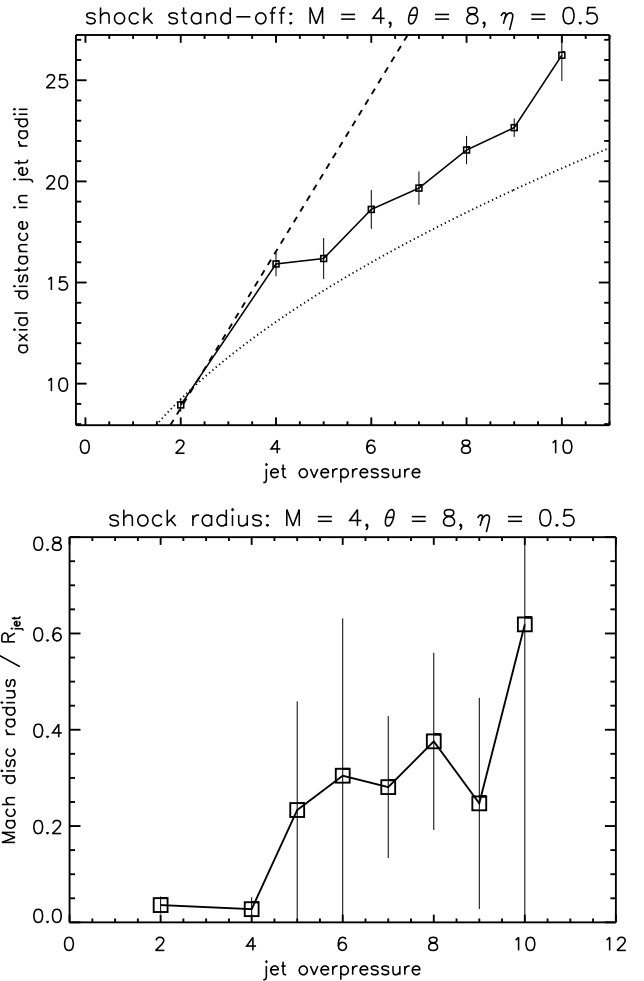


**Figure 15.** Dependence on jet/ambient pressure ratio. The distance of the first shock along the jet axis (upper) and Mach disc radius (lower panel) as a function of overpressure for half-opening  $\theta = 8^\circ$  in units of the jet radius. The density ratio is  $\eta = 0.5$ . The error bars were determined from a root-mean-square fit covering the final 20 time units in order to account for oscillations.

## 4 DISCUSSION

### 4.1 The general trends

The opening angle of modern manufactured jets is variable, being altered during flight to maximize thrust. In planetary and cometary jets, a fissure can be smoothed and re-shaped by abrasive forces on the walls. In astrophysical jets, on the other hand, a sharp discontinuity is not expected. However, a nozzle with an effective opening angle could be a viable approximation when an expanding jet propagates down a steep gradient in confining pressure. As it enters from a gravitationally bound core into an unbound medium, the opening jet would then overexpand. Such a scenario would correspond to a core undergoing Bondi accretion.

The analysis here has taken, as a starting point, the results of previously derived analytical approximations for  $\theta = 0$  for which the Mach number and overpressure could be treated as independent variables. Here, we add  $\theta$  as a third independent variable and make power-law estimates. It should be remarked that these parameters can be independently prescribed at the nozzle in the code. However,



they are likely to be closely related in practice depending on how the flow arose and developed prior to the exit.

The two major predicted quantities are the stand-off distance and the radius of the first shock. It is found that the shock location lies farther from the nozzle for larger opening angles. However, this is generally confined to the regular reflection regime at small angles.

At angles exceeding a critical angle, the first shock takes the form of a transverse disc that increases in radius for higher opening angles. Moreover, the shock stand-off distance decreases.

The above results are clearly explained as due to two effects. First, at small angles, the added divergence beyond that caused by the overpressure delays the subsequent convergence. Second, in contrast, the Mach disc location is approximately determined by where the momentum flux is reduced to that of the ambient pressure. Hence, a larger spread in this flux results in a stand-off shock located closer to the nozzle.

Our simulations also revealed that when the overpressure is set to a large value, the location of the Mach disc is not sensitive to the opening angle. This is because the flow pattern is predominantly determined by the much larger expansion due to the jet pressure.

## 4.2 Jet disruption

Overviews of the observations and theory are available for astrophysical jets in general (Smith 2012), young stars (Ray & Ferreira 2021), and AGN jets in particular (Boettcher, Harris & Krawczynski 2012). Recent progress in computer simulations of protostellar jets is summarized in Lynch, Smith & Glover (2020) and for AGN jets in Martí (2019).

Radio galaxies are now divided into three very broad classes. The original division was between edge-brightened FR II and edge-darkened FR I (Fanaroff & Riley 1974). The reason for this original dichotomy between FR II and FR I sources has remained controversial. Hypotheses involve (1) the influence of the jet Mach number (Bicknell 1985), (2) the accretion rate since it controls the jet power and penetration (Müller et al. 2004), (3) the black hole spin which triggers a magnetic switch (Meier 1999), and (4) hydrodynamic or magnetohydrodynamic instabilities (e.g. Tchekhovskoy & Bromberg 2016).

In the meantime, the FR 0 type has been added, representing a large number of relatively small radio sources, possibly due to youth, disruption, or low momentum flux. These compact radio galaxies may be youthful with energies comparable to the general FR populations (Readhead et al. 1996; Taylor 2003; Costa et al. 2024; Marques et al. 2024). However, there is also evidence that others are older and frustrated (Miranda Marques et al. 2025).

Jets from young stars are also classified in relation to the evolutionary stage of the driving star. Molecular jets are associated with the adolescent stars, in which the outflow penetrates through a narrow channel. In contrast, atomic jets are associated with the later Class 2 objects. These more exposed jets exhibit a trend for widening with age (Hsieh et al. 2017) although an outflow may be better described as a collimated wind. In addition, there is an intermediate stage, where well collimated jets are also found which can possess both molecular and atomic signatures.

We investigate here the role that opening angle could play. We consider a fixed Mach number and an overpressure close to unity so that the dependence on opening angle can be isolated. This situation is envisaged to arise when an expanding pressure-matched jet exits from a dense gravitationally bound core into an unbound uniform medium. The transition must be sufficiently sharp for this to be a valid approximation.

In the present context, a classical FR II double radio source is powered by jets in which the opening angle is small. The pressure within such a jet with a small opening angle and low over pressure would adjust to the external pressure gradient. Then, compression waves induced at the nozzle edge may be sufficiently weak so as not to steepen into disruptive shocks. The result is a smooth exit from a central confining core, such as shown in panels (a) and (b) of Fig. 2.

The resulting near-field flow pattern as the jet exits from the core depends on how the jet has expanded over large distances within the core. For example, a laminar free jet with  $\theta > 1/M_{jet}$  where  $\theta$  is measured in radians, may propagate without dissipation. until it enters a region where it becomes pressure confined. Shocks are then expected as the jet adjusts (Killeen & Bicknell 1988). For a pressure-matched jet, we would expect that the jet remains in causal contact with the surroundings if  $\theta < 1/M_{jet}$ , or, in the relativistic case  $\Gamma_{jet}\theta < 1$  where  $\Gamma$  is the Lorentz factor (Clausen-Brown et al. 2013).

In our present interpretation, to avoid shock dissipation of kinetic energy requires not only the causal contact prior to the exit from the core but also a sufficiently small opening angle to ensure a very weak oblique compressions. This condition was placed in the present context by Smith (1982) where an adiabatic jet that propagates down a pressure-confining atmosphere with pressure  $p_a \propto Z_a^{-q}$  was assumed where  $Z_a$  is the axial distance from the central source.

Given a jet radius and Mach number,  $r_j$  and  $M_j$ , respectively, as functions of distance  $Z_a$ , it was found that the maximum opening angle, expressed through the gradient, is  $dr_j/dZ_a < 1/M_j$ , corresponds to  $q < 2$ . The exiting jet disrupts for larger values of  $q$  if it has remained pressure confined. For sufficiently large values of  $q$ , the jet would become free (unconfined) if the propagation distance within the core is large. Although a value of  $q > 2.12$  was found previously (Smith 1982), the value is sensitive to the assumed parameters.

In this model, the jets disturbed by Mach discs which bifurcate into spine-sheath structures, as shown in panels (c) and (d) of Fig. 2, would generate the large-scale FR I radio galaxies. The causal contact condition is violated at the nozzle edge. Shock jumps occur on the axis in all cases as opposed to steepening compression waves. One can see, however, that the jets eventually disrupt even at low overpressures. but this occurs far downstream. Thus a jet may remain coherent even with large opening angles due to the recollimation mechanism. Radio galaxies of Type I, however, are a heterogeneous class, consisting of relaxed doubles, X-shaped, turbulent plumes, and narrow and wide angle tails (Smith 2012). Thus, jets which are partially disrupted in the near-field would correspond to the narrow-angle tails which often display deceleration and develop a sheath structure (Katz-Stone et al. 1999; Laing, Canvin & Bridle 2005).

On the large scale, as shown in the top panels of Fig. 3, a repeated shock pattern occurs in the near field but disrupts on the scale of order  $100R_{jet}$ . As discussed by Smith (1982), there is evidence that this is the cause of wide-angle tailed radio galaxies of type FR I. This corresponds to the disruption at a galactic bulge-halo transition (Smith 1982).

Supplementary to the large scale disruption, the formation of a Mach shock disc is catastrophic to the jet propagation. Jet disruption is only associated with the presence of a large Mach disc, as illustrated by the panels (e) and (f) of Fig. 2. The Mach disc reduces the jet to a turbulent plume with subsonic speeds.

We associate these latter turbulent flows with FR 0 radio galaxy (Baldi, Capetti & Massaro 2018; Baldi 2023). The FR 0 type consists of a large number of small radio sources. Various potential models are being discussed including undeveloped radio galaxies and low momentum flux. Some may be older and frustrated, which would fit

into the picture developed here since it is only the kinetic efficiency which is mollified by the wide jet opening.

The ability for a jet to survive intact depends on the growth rate and advection speed of surface disturbances. The latter are advected downstream at roughly the Kelvin–Helmholtz speed which is closely correlated to the initial advance speed of the working surface. Space–time diagrams confirm this for the under-expanded jets presented here with  $\kappa = 1$  and  $\theta = 16^\circ$ , as shown in Fig. 16. These diagrams display the jet pressure along the axis at all times and so highlight the propagation speed of the initial bow shock and subsequent shock patterns.

The lower panel of Fig. 16 shows that the untouched ambient medium towards the lower right is present to much later times for a high density jet with  $\eta = 10$ . It is also found that the internal jet pattern propagates at a similar speed across the simulated region. This jet does spread, as seen by the tracer field, with a full opening angle of  $\sim 6^\circ$  (see Fig. 17, lower panel).

On the other hand, the top low density version with  $\eta = 0.1$ , also maintains an inner Mach disc but hardly evolves downstream subsequently. This light jet is also the more powerful jet for the given Mach number and pressure. Hence, the more powerful jets, due to lower densities, are also less prone to disruption. Three dimensional simulations are needed at these distant downstream regions, far beyond the stand-off distance, to investigate thoroughly.

### 4.3 The supersonic condition

It is well-known that there is a critical angle for an oblique shock to sweep over a planar surface which separates direct reflection off the surface from the insertion of a Mach stem and triple point (see p206 of Courant & Friedrichs 1948). The angle depends on the specific heat ratio and is  $41^\circ$  for  $\gamma = 5/3$  (see Hansen et al. (2015) and Hartigan et al. (2016) for a review and an astrophysical application).

In the present jet context, we find a critical half-opening angle of  $16^\circ$  for the jet entering a uniform ambient medium beyond which a part of the jet will suffer a strong shock through a Mach disc. This angle was found to be independent of the Mach number in the above analysis. To confirm this interesting outcome, we have carried out equivalent series of runs for Mach 10, holding  $\kappa = 1$ . Fig. 18 demonstrates that the  $16^\circ$  transition angle remains valid. In addition, we find that the radius of the Mach shock disc increases proportional to the Mach number. The height of the Mach disc can be approximately represented by the formula

$$H_{\text{MD}} \sim 0.0475 \times M \times (\theta - 16)_{+}^{1/2}. \quad (12)$$

This is valid for  $\kappa = 1$  and for  $\theta > 16^\circ$ . Hence, we have uncovered a simple diagnostic, relating flow pattern to opening angle which can be explored.

## 5 CONCLUSIONS

We have performed and analysed hydrodynamic simulations of supersonic jets that are underexpanded or overpressured. We take adiabatic gases and eject the jet from a circular nozzle into a large uniform gas reservoir. Our interest is in the near-field, studying the emerging shock patterns well after the jet has vacated a channel through the reservoir.

The influence of the opening angle is the subject of this work. This is a follow-up to works on the overpressure and Mach number. We explore ranges of the three parameters here.

The simulations are not intended to model a particular type of jet flow. In specific approaches, we would need to add on some

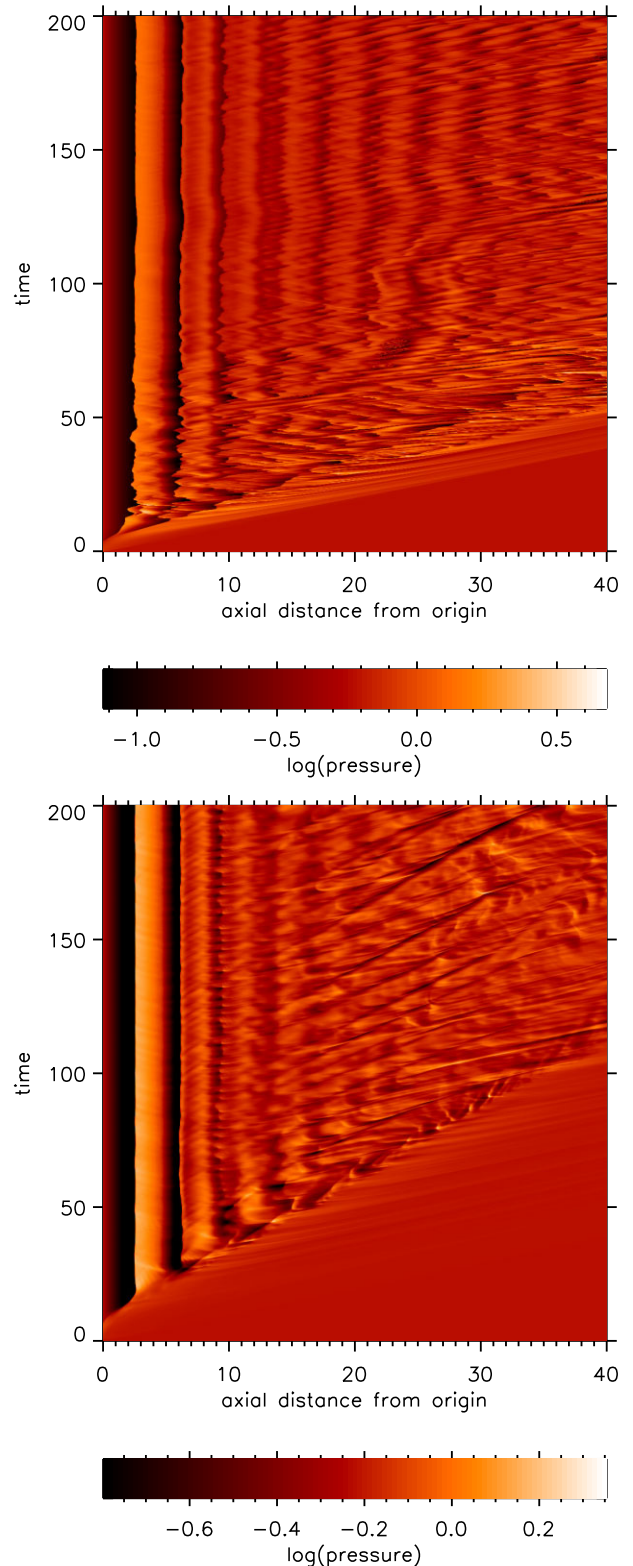


**Figure 16.** Space–time diagram for Mach 2 jets with  $\kappa = 1$ ,  $\theta = 16^\circ$  and with initial density ratios of  $\eta = 0.1$  (upper) and  $\eta = 10$  (lower panel). The distribution of the pressure along the jet axis (x-axis) is shown as function of the time (y-axis). Length-scale is in units of the jet radius.

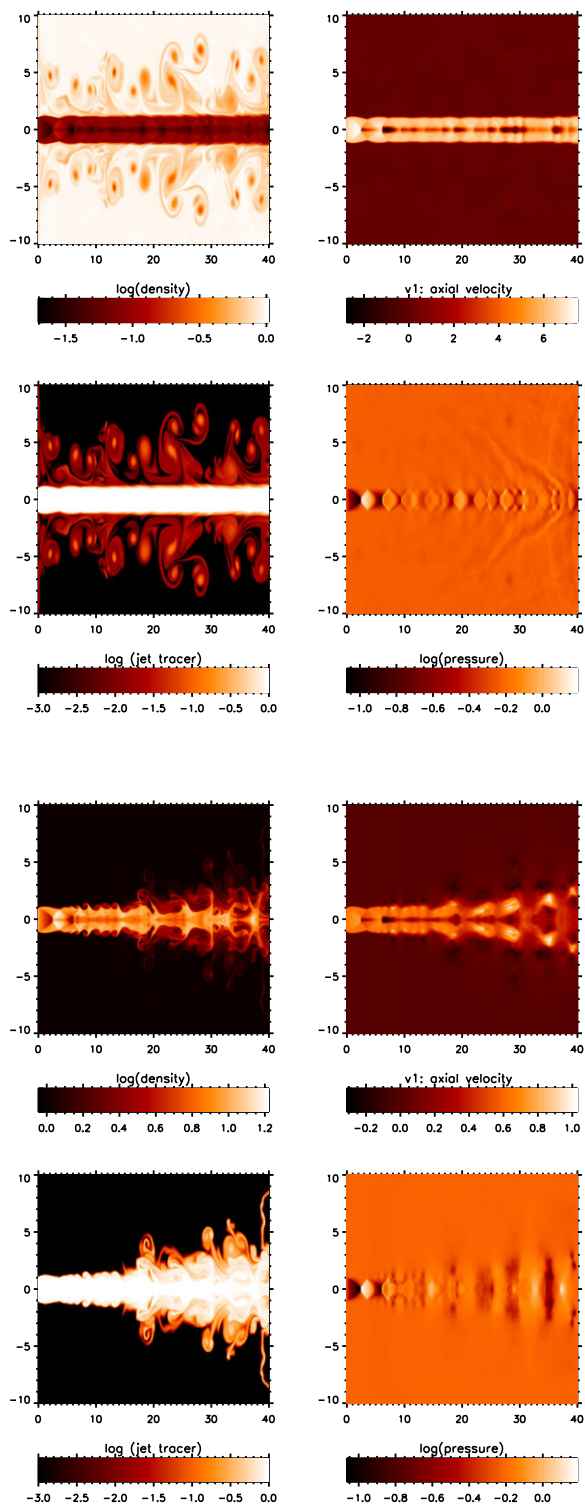


**Figure 17.** The physical parameters for Mach 2 jets with  $\kappa = 1$  and with initial density ratios of  $\eta = 0.1$  (upper) and  $\eta = 10$  (lower panel). The distribution of the pressure along the jet axis ( $x$ -axis) is shown as function of the time ( $y$ -axis). Length-scale is in units of the jet radius.

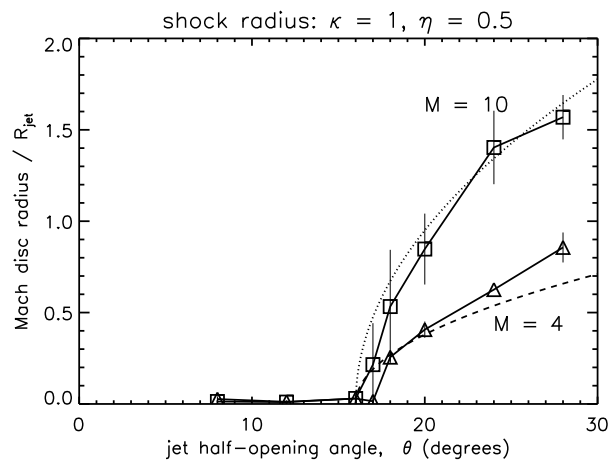


**Figure 18.** The radius of the Mach shock disc as a function of the half-opening angle,  $\theta$ , for an overpressure  $\kappa = 1$  for jets with Mach numbers of 4 (square symbols) and 10 (triangles), density  $\eta = 0.5$ , as measured after 200 time units. The error bars correspond to the root-mean-square spread over the final 20 time units. The superimposed lines are derived from equation (12).

physics to the dynamics. That may include chemistry, magnetic fields, dust, gravity, and relativity. However, we uncover a number of flow patterns that may prompt focused studies of classes of jets.

The fundamental results are as follows.

1. For fixed Mach number and pressure, regular reflection is maintained below a critical half-opening angle.
2. The location where the stand-off shock occurs moves away from the inlet as the opening angle increases.
3. Near the critical angle, jittering and oscillation in the pattern are sustained and the pattern can vary between a small Mach disc and a conical shock. A high velocity sheath separates the Mach disc and spine from the ambient medium.
4. As the angle is further increased, a wide Mach disc traverses the expanded jet and the shock is located closer to the nozzle.

Shock locations and shock front dimensions have been modelled with linear relationships that extend quite well from the formulae derived for parallel flow jets. However, these are empirical relations that are complicated to model for the higher overpressures in which 2D flow properties and oscillations are apparent.

Combining with previous studies, we note that for a given small overpressure and opening angle, an increasing Mach number generates a sequence of flow patterns from (i) a destructive Mach disc, to (ii) a series of shock diamonds and Mach discs and then to (iii) a stable steady flow with weak internal shocks. This is one means of generating flows in which jet power and flow pattern are correlated, in the sense observed for radio galaxies in the extended Fanaroff and Riley classes, FR 0, FR I, and FR II (Fanaroff & Riley 1974; Baldi et al. 2018).

There is a critical half-opening angle of  $16^\circ$  for a jet entering a uniform ambient medium beyond which a Mach disc will appear. This angle is independent of Mach number and has been established here for a specific heat ratio of  $5/3$ . This implies that there is a simple diagnostic which relates flow pattern to opening angle. This may relate a kinetically efficient jet in which supersonic flow is preserved from one in which a subsonic spine is produced. We suspect that similar properties arise for both relativistic and magnetohydrodynamic jets.

## ACKNOWLEDGEMENTS

We thank the referee for useful comments. BR thanks Mata Amritanandamayi for encouragement.

## DATA AVAILABILITY

No new observational data were generated or analysed in support of this research. Simulation source files are available on request. The data underlying this article will be shared on reasonable request to the corresponding author.

Complete 1000-frame movies of a selection of simulations are available in the Zenodo repository, at <https://zenodo.org/records/14174127> or through DOI 10.5281/zenodo.14174127.

## REFERENCES

- Adamson T. Jr, Nicholls J. A., 1959, *J. Aerosp. Sci.*, 26, 16
- Baldi R. D., 2023, *A&AR*, 31, 3
- Baldi R. D., Capetti A., Massaro F., 2018, *A&A*, 609, A1
- Bicknell G. V., 1985, *Proc. Astron. Soc. Aust.*, 6, 130
- Boettcher M., Harris D. E., Krawczynski H., 2012, *Relativistic Jets from Active Galactic Nuclei*. Wiley, Berlin
- Clausen-Brown E., Savolainen T., Pushkarev A. B., Kovalev Y. Y., Zensus J. A., 2013, *A&A*, 558, A144
- Costa A. et al., 2024, *A&A*, 682, L19
- Courant R., Friedrichs K. O., 1948, *Supersonic Flow and Shock Waves*. Interscience Publishers, New York
- Davis C. J. et al., 2009, *A&A*, 496, 153
- Duronio F., Villante C., De Vita A., 2023, *Energies*, 16, 6471
- Fanaroff B. L., Riley J. M., 1974, *MNRAS*, 167, 31P
- Franquet E., Perrier V., Gibout S., Bruel P., 2015, *Prog. Aerosp. Sci.*, 77, 25
- Hada K., Asada K., Nakamura M., Kino M., 2024, *A&AR*, 32, 5
- Hansen E. C., Frank A., Hartigan P., Yirak K., 2015, *High Energy Density Phys.*, 17, 135
- Hartigan P. et al., 2016, *ApJ*, 823, 148
- Hsieh T.-H., Lai S.-P., Belloche A., 2017, *AJ*, 153, 173
- Katz-Stone D. M., Rudnick L., Butenhoff C., O'Donoghue A. A., 1999, *ApJ*, 516, 716
- Killeen N. E. B., Bicknell G. V., 1988, *ApJ*, 324, 198
- Kovalev Y. Y., Pushkarev A. B., Nokhrina E. E., Plavin A. V., Beskin V. S., Chernoglazov A. V., Lister M. L., Savolainen T., 2020, *MNRAS*, 495, 3576
- Laing R. A., Canvin J. R., Bridle A. H., 2005, in Sjouwerman L. O., Dyer K. K., eds, *X-Ray and Radio Connections*. NRAO, Charlottesville, USA, p. 7.02
- Levinson A., Globus N., 2017, *MNRAS*, 465, 1608
- Lynch C. J. R., Smith M. D., Glover S. C. O., 2020, *MNRAS*, 491, 3082
- Marques B. L. M., Rodríguez-Ardila A., Fonseca-Faria M. A., Panda S., 2024, preprint (arXiv:2411.03130)
- Martí J.-M., 2019, *Galaxies*, 7, 24
- Martí J. M., Perucho M., Gómez J. L., 2016, *ApJ*, 831, 163
- Meier D. L., 1999, *ApJ*, 522, 753
- Michel U., 2011, *49th AIAA Conf. Vol. AIAA-2011-0226, The Benefits of Variable Area Fan Nozzles on Turbofan Engines*. Orlando, Florida
- Mignone A., Bodo G., Massaglia S., Matsakos T., Tesileanu O., Zanni C., Ferrari A., 2007, *ApJS*, 170, 228
- Miranda Marques B. L., Rodríguez-Ardila A., Fonseca-Faria M. A., Panda S., 2025, *ApJ*, 978, 16
- Müller S. A. H., Haas M., Siebenmorgen R., Klaas U., Meisenheimer K., Chini R., Albrecht M., 2004, *A&A*, 426, L29
- Mundt R., Fried J. W., 1983, *ApJ*, 274, L83
- Mundt R., Ray T. P., Raga A. C., 1991, *A&A*, 252, 740
- Ray T. P., Ferreira J., 2021, *New Astron. Rev.*, 93, 101615
- Readhead A. C. S., Taylor G. B., Xu W., Pearson T. J., Wilkinson P. N., Polatidis A. G., 1996, *ApJ*, 460, 612
- Smith M. D., 1982, *ApJ*, 259, 522
- Smith M. D., 1994, *ApJ*, 421, 400
- Smith M. D., 2012, *Astrophysical Jets and Beams*. Cambridge Univ. Press, Cambridge
- Smith M. D., Keogh T. L. R., 2022, *MNRAS*, 516, 2757
- Smith M. D., Norman C. A., 1981, *MNRAS*, 194, 771
- Smith M. D., Richards C., 2023, *MNRAS*, 526, 3407
- Tam C. K. W., 1995, *Ann. Rev. Fluid Mech.*, 27, 17
- Taylor G. B., 2003, *New Astron. Rev.*, 47, 585
- Tchekhovskoy A., Bromberg O., 2016, *MNRAS*, 461, L46
- Toro E. F., Spruce M., Speares W., 1994, *Shock Waves*, 4, 25

This paper has been typeset from a  $\text{\TeX}/\text{\LaTeX}$  file prepared by the author.